AGU PUBLICATIONS

Tectonics

RESEARCH ARTICLE
10.1002/2013TC003481

Key Points:
- A method to evaluate section restorations with thermochrone data is proposed
- The method is presented through the case of the Pyrenean ECORS cross-section
- We propose the method to be applicable in other geological settings

Supporting Information:
- Figure S1
- Table S1–S2
- Text S1

Correspondence to:
Z. Erdős,
zoltan.erdos@geo.uib.no

Citation:
Erdős, Z., P. van der Beek, and R. S. Huismans (2014), Evaluating balanced section restoration with thermochronology data: A case study from the Central Pyrenees, *Tectonics*, *33*, 617–634, doi:10.1002/2013TC003481.

Received 15 NOV 2013
Accepted 28 MAR 2014
Accepted article online 3 APR 2014
Published online 6 MAY 2014

Evaluating balanced section restoration with thermochronology data: A case study from the Central Pyrenees

Zoltán Erdős[1,2], Peter van der Beek[2], and Ritske S. Huismans[1]

[1]Department of Earth Science, University of Bergen, Bergen, Norway, [2]Institut des Sciences de la Terre (ISTerra), Université Joseph Fourier, Grenoble, France

Abstract We present a new method that can be used to quantitatively evaluate the consistency between balanced section restorations and thermochronological data sets from orogenic belts. We have applied our method to a crustal-scale area-balanced cross-section restoration along a profile in the Central Pyrenees. This restoration is well constrained and supported by a wide variety of geological and geophysical data. Moreover, an extensive thermochronological data set has been collected independently in the area. We use the structural-kinematic software 2D-Move™ to constrain a set of velocity fields that describes the kinematics of the Central Pyrenees. Using these velocity fields as input for the thermokinematic code PECUBE, we derive predictions of the thermal history and a range of thermochronometric ages for the modeled area. We find that the kinematic history of the belt as inferred from section balancing is in good agreement with the published thermochronological data. High-temperature (zircon fission-track and K-feldspar Ar-Ar) data constrain the thermal structure of the belt as well as the timing of underplating. Low-temperature (apatite fission-track and (U-Th)/He) data require late synorogenic sedimentary burial of the southern flank of the Pyrenees between late Eocene (40 Ma) to late Miocene (9 Ma) times, consistent with previous studies, and imply that no such burial occurred on the northern flank.

1. Introduction

Crustal-scale balanced cross-section restorations synthesize our knowledge about the structural-kinematic history of a mountain belt. Although the method had been used previously, the basic principles of creating a balanced cross section were thoroughly discussed for the first time by *Dahlstrom* [1969]. Crustal-scale restorations require understanding not just the present-day geology and the history of the area in question but also the processes acting on the deep structures as well as those playing a role in the formation of topography. The synthesis of all available geological and geophysical data is essential to allow maximum constraint on the restoration. Section restorations based on deep seismic profiles have been published for the Alps [e.g., *Roure et al.*, 1996; *Schmid et al.*, 1996], the Canadian Rocky Mountains [e.g., *Cook et al.*, 1992], and the Pyrenees [e.g., *Muñoz*, 1992; *Séguret and Daignières*, 1986], while, more recently, restorations based mainly on geologic data have been compiled for the Andes [e.g., *McQuarrie*, 2002; *McQuarrie et al.*, 2008] and the Himalaya [e.g., *DeCelles et al.*, 2001; *Long et al.*, 2011; *Robinson et al.*, 2006] among others.

Additional and independent constraints on orogen kinematics are provided by thermochronology data, which record exhumation of rocks in response to tectonic thickening, rock uplift, and erosion [e.g., *Braun et al.*, 2006; *Reiners and Brandon*, 2006]. Such data can therefore, in principle, be used to discriminate between competing kinematic models for orogens [e.g., *Herman et al.*, 2010; *Robert et al.*, 2011] or to provide additional temporal constraints on balanced section restorations [e.g., *Long et al.*, 2012; *McQuarrie et al.*, 2008]. Conversely, the kinematics implied by such restorations can be used to predict thermal history and thermochronologic age patterns in, for instance, foreland fold-and-thrust belts [*Lock and Willett*, 2008; *ter Voorde et al.*, 2004].

However, these two approaches to decipher orogen kinematics generally remain detached from each other and no quantitative, internally consistent framework exists as yet to fully integrate the two. In this study, we propose such a methodology and quantitatively evaluate the consistency of a balanced cross-section restoration of the Central Pyrenees, based on *Muñoz* [1992] and *Beaumont et al.* [2000], with independent thermochronological data for a range of systems with different closure temperatures. The Central Pyrenees constitute an ideal test case to validate our methodology, as the existing balanced cross section is well

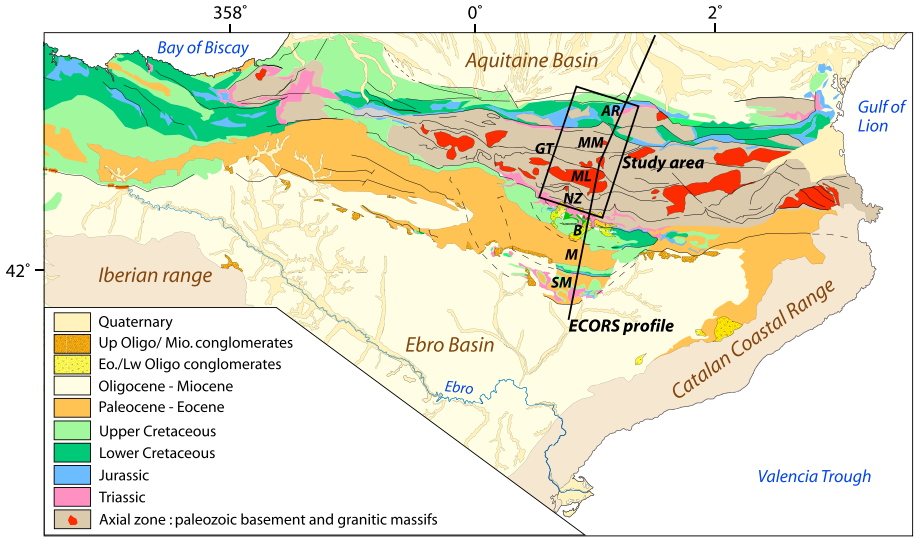

Figure 1. Geological map of the Pyrenees. The black line represents the ECORS deep seismic profile along which the balanced cross section of Figure 2 was constructed, and the box indicates the boundaries of the thermokinematic model. AR: Arize block, MM: Marimaña massif, ML: Maladeta massif, NZ: Nogueres Zone, GT: Gavarnie thrust B: Bóixols, M: Montsec, and SM: Sierras Marginales [redrawn after *Fillon and van der Beek*, 2012].

constrained by a wide range of geological and geophysical data but does not incorporate the more recently collected extensive thermochronological database (see details and references in the next section). The method can be applied to other orogenic belts where fewer constraints exist to evaluate the consistency of proposed cross-section restorations with available thermochronology data or to provide additional temporal constraints on such restorations.

2. Geological Setting

2.1. The Pyrenean Orogen

The Pyrenees (Figure 1) are a collisional orogen formed by Late Cretaceous (90 Ma) to early Miocene (20 Ma) convergence between the Iberian and European Plates [*Roest and Srivastava*, 1991; *Rosenbaum et al*., 2002; *Vissers and Meijer*, 2012]. According to these plate-kinematic analyses, the convergence rate reached its peak during the Eocene to Oligocene (50–20 Ma). The range is dominated by inversion tectonics [*Muñoz et al*., 1986] owing to thrusting along preexisting extensional structures (Figure 2). These structures were originally formed during Triassic to Cretaceous rifting and transtension associated with anticlockwise rotation of the Iberian Plate with respect to Europe and consequent opening of the Bay of Biscay [*Roest and Srivastava*, 1991; *Rosenbaum et al*., 2002].

The asymmetrical Pyrenean orogen resulted from northward underthrusting of the Iberian crust below the European crust, resulting in a wide southern prowedge and a narrower northern retrowedge (Figure 2). In the center of the belt, the Axial Zone comprises a south vergent antiformal stack of upper crustal thrust sheets [*Muñoz*, 1992]. The Axial Zone is flanked by the South Pyrenean Unit toward the south and the North Pyrenean Unit toward the north, respectively. The South Pyrenean Unit is a fold-and-thrust belt consisting of Mesozoic and Cenozoic sedimentary rocks, while in the North Pyrenean Unit, basement and cover rocks form north vergent thrust sheets and pop-up structures [*Muñoz*, 1992; *Capote et al*., 2002]. The Pyrenees are flanked by the Ebro and the Aquitaine foreland basins toward the south and north, respectively (Figures 1 and 2).

Our study area is located in the Central Pyrenees, along the Etude Continentale et Océanique par Reflexion et Refraction Sismique (ECORS) deep seismic profile [*ECORS Pyrenees Team*, 1988] (Figure 1). Although we have used the entire section to constrain the velocity fields in the structural-kinematic model, the thermokinematic models cover only the Axial Zone and the North Pyrenean Unit, as the bulk of the published thermochronological data has been collected in these areas.

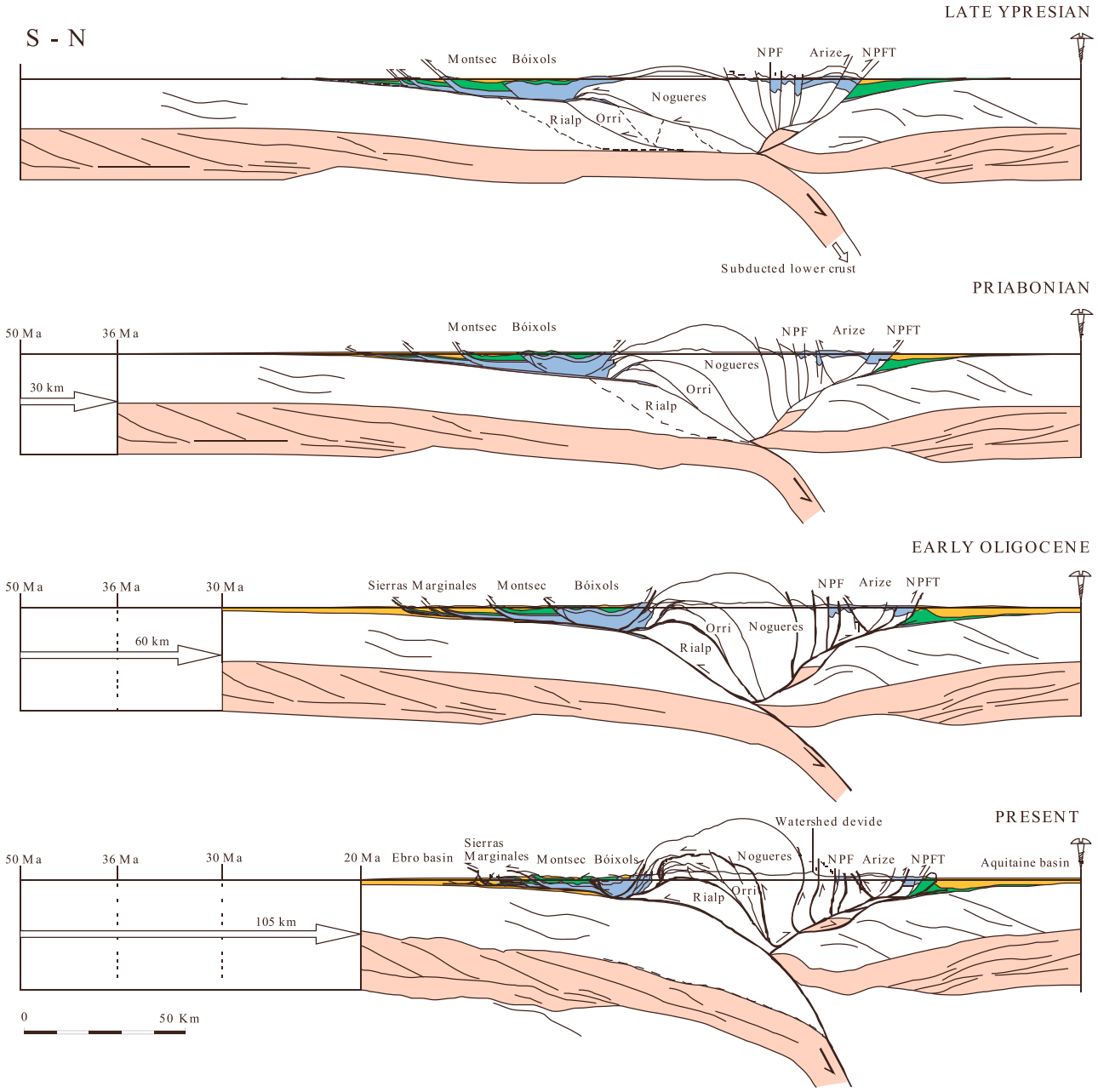

Figure 2. Four time slices (between 50 Ma and Present) of the crustal-scale area-balanced cross-section restoration of the Central Pyrenees along the ECORS deep-seismic profile by *Muñoz* [1992] and *Beaumont et al.* [2000]. NPF: North Pyrenean Fault; NPFT: North Pyrenean Frontal Thrust. Figure modified from *Beaumont et al.* [2000].

2.2. Structural Evolution of the Pyrenees

The kinematics are well constrained in the South Pyrenean Unit as the tectonic evolution is exceptionally well recorded by syntectonic sediments [e.g., *Muñoz*, 1992; *Puigdefabregas et al.*, 1986, 1992; *Vergés and Muñoz*, 1990]. The evolution of the Axial Zone has been inferred from correlation of its thrust sheets with those in the South Pyrenean Unit, while that of the North Pyrenean Unit is less well constrained.

The South Pyrenean Unit is made up of three thin-skinned thrust sheets (from south to north, the Sierras Marginales, Montsec, and Bóixols; Figure 2), which have been emplaced on top of a detachment located in Upper Triassic evaporites in a southward propagating deformation sequence [*Muñoz*, 1992]. The Bóixols thrust was activated during the Maastrichtian (from ~70–65 Ma), as indicated by the overlying syntectonic

sequences. Deformation stepped onto the Montsec thrust during the Ypresian (~55 Ma). Finally, the Sierras Marginales unit was activated between the early and late Eocene (50–40 Ma). The forward propagation of deformation in the South Pyrenean Unit was modified during the last (late Eocene) stage of the thrust belt evolution by break-back reactivation of the older thrusts and by the development of new, minor out-of-sequence thrusts, possibly in response to rapid accumulation of syntectonic sediments [*Capote et al*., 2002; *Fillon et al*., 2013]. The northern fault contact of the Bóixols thrust sheet is the Morreres back thrust, which has been interpreted as a passive roof thrust [*Muñoz*, 1992].

The antiformal stack of the Axial Zone involves upper to middle crustal rocks and consists of three thrust sheets: Nogueres, Orri, and Rialp (Figure 2). These units were initially juxtaposed and separated by extensional faults before the onset of thrusting [*Muñoz*, 1992]. The highly eroded Nogueres thrust sheet is the uppermost of the three units. Its frontal tip has been preserved in the southern limb of the antiformal stack and is known as the Nogueres Zone, while its root-zone crops out in the northern part of the Axial Zone [*Muñoz*, 1992]. Thrusting of the Nogueres unit over the Orri unit took place between the Late Cretaceous and the early Eocene (90–50 Ma). Deformation subsequently stepped onto another Mesozoic extensional fault, causing the Orri unit to overthrust the Rialp unit during the middle to late Eocene (50–36 Ma). Finally, deformation shifted again to create the Rialp thrust sheet between the middle Eocene and the late Oligocene (36–20 Ma) [*Capote et al*., 2002; *Metcalf et al*., 2009].

North of the Axial Zone in the North Pyrenean Unit, very steep, north vergent thrust sheets, and pop-up structures involve basement and Mesozoic cover rocks in both their footwalls and hanging walls. Most of the orogenic displacement in the North Pyrenean Unit occurred along the North Pyrenean Frontal Thrust, while the steep faults observed in the basement were probably not strongly reactivated during the Pyrenean orogeny. They may represent either contractional Hercynian structures or younger, extensional pre-Pyrenean fault zones [*Capote et al*., 2002]. As the timing of the deformation along the subvertical faults is very difficult to assess, the structural history of North Pyrenean Unit remains controversial [*ECORS Pyrenees Team*, 1988].

2.3. Thermochronology Data

Altogether, 72 published thermochronometric ages have been used from 48 different locations to test the predictions of the thermokinematic models: 39 apatite fission-track (AFT) ages, 26 apatite (U-Th)/He (AHe) ages, 4 zircon fission-track (ZFT) ages, and 3 time-temperature models extracted from K-feldspar $^{40}Ar/^{39}Ar$ degassing experiments [*Fitzgerald et al*., 1999; *Gibson et al*., 2007; *Metcalf et al*., 2009; *Sinclair et al*., 2005]. The samples were collected along two age-elevation profiles in the Maladeta massif, one profile in the Barruera block, one profile in the Marimaña massif, and one profile in the Lacourt massif (Figures 1 and 3). Individual samples were also collected from the Nogueres Zone along the southernmost edge of the Axial Zone. The Maladeta and Barruera profiles are located in the Orri thrust sheet, whereas the Marimaña profile is located in the Nogueres thrust sheet, in the hanging wall of the Gavarnie thrust (Figure 1). The Nogueres samples come from the southern frontal zone of the Nogueres thrust sheet. The Lacourt profile is located within the southern part of the Arize block (Figure 3) and is the only profile located in the North Pyrenean Unit. The samples in the Maladeta, Barruera, Marimaña, and Lacourt profiles were collected from Hercynian granitic plutons, while the samples in the Nogueres Zone are from Cambrian to Triassic volcanic rocks.

The profiles line up along two different trends (Figure 3). The Nogueres, Barruera, Maladeta, and Marimaña profiles show an almost vertical age-elevation trend at elevations above 1500 m, suggesting rapid exhumation around 30–40 Ma [e.g., *Fillon and van der Beek*, 2012; *Fitzgerald et al*., 1999; *Sinclair et al*., 2005]. The lower elevation samples of these profiles line up along a gentler slope on the age-elevation plots, suggesting decreased erosion rates from 30 Ma to around 20 Ma. The Lacourt profile spans only a few hundred meters of relief and does not show a clear age-elevation relationship; AFT ages for these samples are 50–55 Ma, significantly older than those from the other profiles.

The Barruera profile is located very close to the western Maladeta profile, but both the AFT and the AHe samples yield systematically younger ages than samples in the Maladeta profile from similar elevations. The significance and the cause of this difference are not yet fully understood. Recently, *Rushlow et al*. [2013] have suggested that a late stage of focused denudation affected the southern flank of the Axial Zone in response to either disturbance of the critical taper by syntectonic sedimentation in the South Pyrenean Unit or a regional climate shift.

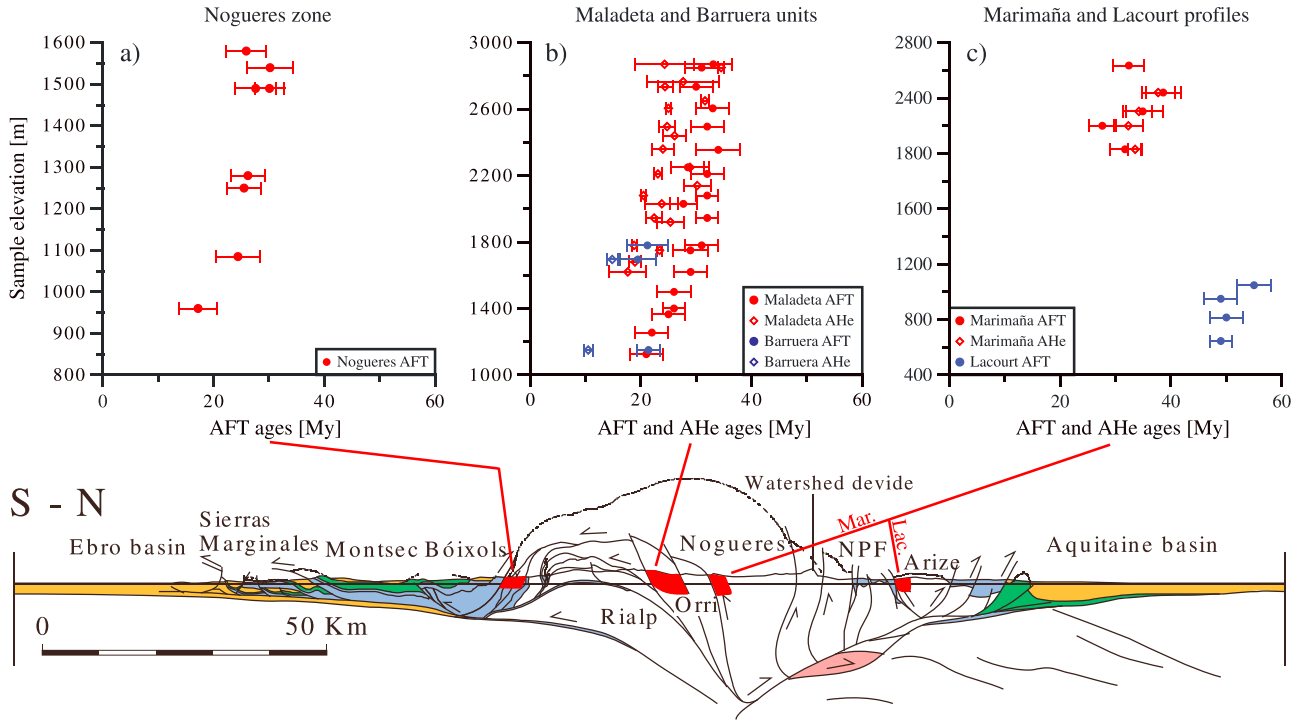

Figure 3. Apatite fission track and apatite (U-Th)/He ages along the ECORS deep seismic profile published by *Fitzgerald et al.* [1999], *Sinclair et al.* [2005], *Gibson et al.* [2007], and *Metcalf et al.* [2009], plotted together on age-elevation plots [section modified from *Beaumont et al.*, 2000]. Error bars for AHe and AFT ages represent 1σ error. Note the different elevation scales.

Samples in the Marimaña profile that provided both AFT and AHe ages yielded AHe ages that are within uncertainty of or slightly older than the respective AFT ages [*Gibson et al.*, 2007]; this is also the case for some of the Maladeta profile samples reported by these authors. The significance of these ages also remains unclear; they might have been affected by either minute (U-Th)-rich inclusions or implantation of He from surrounding minerals but could also indicate extremely rapid cooling through both the AFT and AHe closure temperatures. We have therefore chosen to include all available data in the data set that we will compare to our forward model predictions.

Metcalf et al. [2009] modeled time-temperature paths from K-feldspar $^{40}Ar/^{39}Ar$ thermochronometry in the Maladeta Pluton. Three analyzed samples yielded similar thermal histories, showing a heating phase until around 40–50 Ma, interpreted as due to tectonic burial beneath the Nogueres thrust sheet in the footwall of the Gavarnie thrust, before rapid exhumational cooling. The K-feldspar $^{40}Ar/^{39}Ar$ models do not constrain the end of exhumation as the lowest-temperature $^{40}Ar/^{39}Ar$ step yielded an age of ~20 Ma [*Metcalf et al.*, 2009]. The peak burial temperature for the two lower-elevation samples is around 280°C, while for the highest elevation sample it is around 175°C. The latter estimate is, however, probably less well constrained as it is at the lowermost end of the sensitivity of the K-feldspar $^{40}Ar/^{39}Ar$ thermochronometer [*Metcalf et al.*, 2009].

Sinclair et al. [2005] published four ZFT ages—one from the Nogueres, Barruera, Maladeta, and Marimaña massifs each—that range from 49.3 ± 2.6 Ma to 159 ± 33 Ma, implying that total exhumation since 50 Ma (the starting time of our thermokinematic models) was not sufficient to bring rocks with fully reset ZFT ages to the surface.

3. Methodology

The proposed method links a two-dimensional structural-kinematic restoration model with a three-dimensional thermokinematic model that is capable of predicting cooling ages for a range of thermochronometers (Figure 4). We use velocity fields derived from the structural-kinematic model to advect material in the thermokinematic model. This allows us to predict thermochronometric ages and compare them quantitatively with the available observations. Our method is somewhat similar to the approach presented by *Lock and Willett*

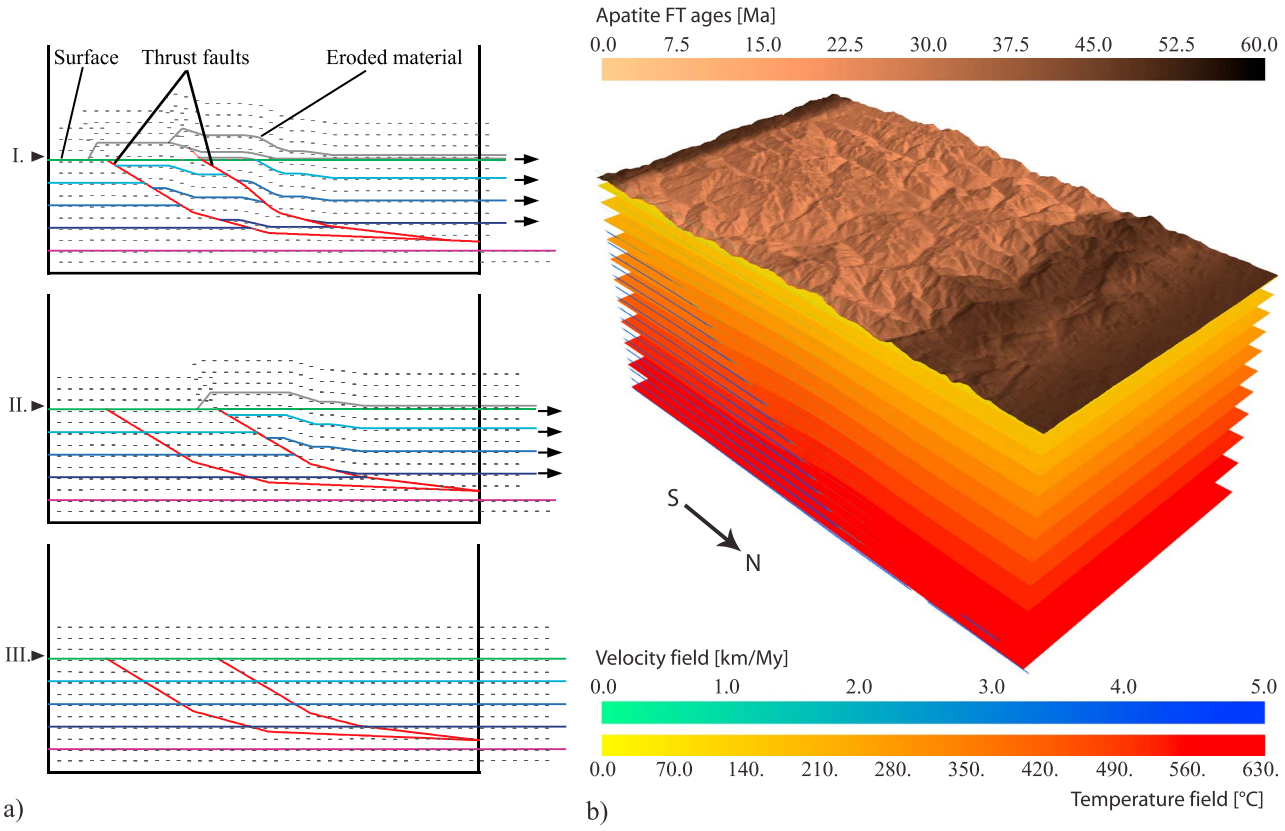

Figure 4. Principles of the method. (a) A velocity field is derived for each time interval of the modeled section restoration using 2D-Move™. A time interval is defined between two consecutive steps (e.g., I and II or II and III) of the restoration. In our synthetic example, the black cloud of points represents a Lagrangean marker field tracking the materials. (b) The velocity fields are subsequently imported in the thermokinematic model PECUBE to predict thermochronometric ages for particles ending up on the surface of the model. These ages can be compared with sample ages obtained from the area.

[2008], who aimed to predict low-temperature thermochronometric ages in fold-and-thrust belts, although our thermokinematic and age-prediction models are significantly more elaborate.

3.1. Calculating Velocity Fields

A conventional section restoration, such as the one presented by *Muñoz* [1992] for the Central Pyrenees (Figure 2), consists of several time slices representing the structure of a crustal section at different times. Extracting kinematics from such a restoration requires tracking particle paths from one time slice to another, which can be achieved by quantitative structural-kinematic modeling packages. As the geological and geophysical constraints on the restoration of the section only apply to the present day, we have chosen to carry out the structural-kinematic modeling starting with this section. Our starting point is thus a model representing the present state of the section that we created using the structural-kinematic modeling software 2D-Move™ (Midland Valley Ltd). Using the constraints derived from the section restoration on the timing and the amount of displacement along the active faults, all the crustal blocks can be moved from their position on any particular time slice to their position on the time slice directly predating it. In theory, this procedure can be repeated for an indefinite number of time slices.

In 2D-Move, the deformation within hanging wall beds resulting from movement over a fault plane can be modeled using various algorithms. We have tested the different available options, but only the simple-shear algorithm proved to be capable of handling the geometric complexity of our model. The algorithm predicts the deformation of the hanging wall using the shape of the underlying fault while leaving the footwall undeformed [*Withjack and Peterson*, 1993]. The deformation fulfills the condition of volume conservation (or area conservation, in case of a 2-D section assuming plane strain) and is calculated according to the "velocity method" [*Waltham and Hardy*, 1995]. This method provides the rate and direction of particle movement in a

model calculated with the "isogon method" of *Waltham* [1989] and shifts the points of the model accordingly [*ter Voorde et al*., 2004]. An alternative option available in 2D-Move is the fault-parallel flow algorithm, which is a more appropriate choice for the reconstruction of individual units within a compressional setting, as it is designed to kinematically model geological structures in the hanging wall where deformation is accommodated by fault-parallel shear [*Egan et al*., 1999]. However, our aim was to model the section reconstruction as a whole, and the fault-parallel flow algorithm is less suitable for this purpose as it operates with angular shear (also known as back shear) to maintain constant bed thickness, which creates significant deformation in the far field [see *Egan et al*., 1999, and references therein].

The input parameters of the simple-shear algorithm are the amount of displacement, the direction of movement along the active fault and the angle of the applied shear. In 2D-Move, movements along different faults cannot be applied simultaneously, which means that all fault motions must be applied sequentially. The order in which fault movements are applied within any particular step of the reconstruction is inconsequential.

Since the simple-shear algorithm leaves the footwall of the active fault undeformed, the flexural-slip unfolding algorithm has been used to simulate the changes in the shape of the main crustal decollement from one time slice to the other. This algorithm divides the section into thin vertical strips that can be freely translated along their boundaries in the vertical direction. With this method, a chosen horizon (in our case the main decollement on the present-day time slice) can be unfolded to a target line (in our case a line following the shape of the decollement on the predating time slice). It is important to note that the flexural-slip unfolding algorithm conserves area.

We have consistently used the simple-shear algorithm with vertical shear direction, as that is the simplest and most reliable option available in 2D-Move. In this setup the displacement isogons (lines joining points with identical displacement vectors) are vertical [*Waltham*, 1989]. This means that the hanging wall is deformed as if it was cut into thin, vertical columns, and translated on top of the undeforming footwall. For the simple-shear algorithm to work properly, the active fault has to extend all the way below the hanging wall. Since the decollement depicted on the reconstruction of Figure 2 ends in a steep subduction zone, it has been smoothly transitioned in our model into a horizontal fault deep in the mantle.

As the deformation of the hanging wall depends on the shape of the active fault below, the extension of the decollement below the northern part of the section induces undesired deformation of the hanging wall north of the S point. To restore this deformation we have used the flexural-slip unfolding algorithm. The 0 m elevation line of the starting time slice is tracked along with the modeled horizons. After resolving all fault-related deformation, we have used this 0 m elevation line as the unfolding horizon. The target horizon is a smooth downward convex line, representing the material eroded during the time interval in question. It is defined so that the area enclosed by this line and the 0 m elevation line of the target time slice is equal to the measured difference in area of the upper crust between the starting and the target time slices. The exact shape of the target line is picked to achieve the best geometrical match between the model and the target restoration (Figure 2).

Tracking of particle motion within the crustal blocks is achieved by the introduction of a marker cloud with unique identifiers for each point in the cloud. These markers are advected along with the material through time. A displacement vector can be derived from the starting and final position of each marker point for each time interval (i.e., the time spent between two subsequent time slices). Subsequently, a velocity field can be created for each time interval by dividing the resulting displacement vectors by the length of the time interval. Note that this approach may lead to velocity fields that largely simplify particle paths within blocks that are moving along curved faults.

A detailed description of the structural-kinematic modeling carried out on the case study of the Central Pyrenees is provided in the supporting information.

3.2. Thermokinematic Modeling

The result of the structural-kinematic modeling consists of a set of velocity fields, each describing the deformation pattern for one time interval of the section restoration. These velocity fields serve as input for the thermokinematic model PECUBE [*Braun*, 2003; see also *Braun et al*., 2012].

PECUBE is designed to solve the three-dimensional heat-transport equation in a crustal block submitted to a specific tectonic and topographic scenario. The code uses a finite-element approach to derive the

Table 1. Reference Thermal and Kinematic Parameters Used in PECUBE Modeling[a]

Parameter	Value
Crustal density	2700 kg m^{-3}
Model thickness	35 km
Thermal diffusivity	25 km^2 Myr^{-1}
Basal crustal temperature	570°C; 600 °C; **630°C**
Sea level temperature	15°C
Atmospheric lapse rate	4°C km^{-1}
Crustal heat production	0.8 μW m^{-3}; **0.95 μW m^{-3}**

[a]Bold values for basal temperature and crustal heat production those used in the reference model and are set to obtain a surface heat flow of 70 mW m^{-2} and a corresponding geothermal gradient of 33°C km^{-1} [e.g., *Fernandez and Banda*, 1989; *Fernandez et al*., 1998; *Fillon and van der Beek*, 2012].

time-temperature (*t-T*) paths of individual rock particles ending up at the surface at the end of the model run. These *t-T* paths are subsequently used to compute apparent ages for a range of thermochronometers, using standard thermochronological age-prediction models [*Braun et al*., 2012].

We have implemented a new feature in PECUBE so that it can use a set of velocity fields as input files for the calculation of particle paths. The standard kinematic input for PECUBE consists, for each modeled time step, of a fault geometry and the velocities of the hanging wall and footwall with respect to the fault [cf. *Braun et al*., 2012]. We have replaced this input by a set of velocity vectors derived from the structural-kinematic model for each time step. The two-dimensional velocity fields derived from the structural-kinematic modeling are extrapolated in the third dimension, normal to the section, to allow direct comparison with the observed thermochronological data and correctly take into account the influence of topography.

Since the calculated *t-T* paths are highly sensitive to surface topography, the predicted thermochronological ages will be affected by the implemented topographic evolution scenario [*Braun*, 2002; *Braun et al*., 2006]. The influence of the surface topography is strongest for thermochronometric systems characterized by low closure-temperature (e.g., apatite fission-track and (U-Th)/He systems) [*Braun et al*., 2006]. Since the paleotopography of a mountain belt is extremely difficult to determine, it is common practice to use the present-day surface topography throughout the modeled time period, thereby supposing topographic steady state [e.g., *Herman et al*., 2010; *Robert et al*., 2011; *Whipp et al*., 2007]. In case this simplification is not sufficient, PECUBE includes a set of options allowing simple parametric amplification or reduction of the topography [e.g., *Glotzbach et al*., 2011; *Valla et al*., 2010]. Basic sedimentation scenarios can also be implemented [*Fillon and van der Beek*, 2012]. These options enable testing different topographic evolution scenarios for the same set of velocity fields. In our models, we have used a digital elevation model of the present-day surface topography downgraded to a resolution of 300 m. The crustal blocks and the deposits have spatially uniform material properties, typical for the continental crust (Table 1). For a more detailed description of the use of PECUBE we refer the reader to *Braun* [2003] and *Braun et al*. [2012].

3.3. Thermochronometric Age Predictions

PECUBE predicts thermochronometric ages from the time-temperature histories of rock particles using forward kinetic models [*Braun et al*., 2012]. Apatite (U-Th)/He (AHe) ages are predicted using the numerical scheme presented in *Wolf et al*. [1998] and the kinetic parameters proposed by *Farley* [2000]. Apatite (AFT) and zircon (ZFT) fission-track ages can be predicted using several different models and parameterizations. For AFT ages, we have used the model presented by *Green et al*. [1989] with kinetic parameters modified by *Stephenson et al*. [2006], while for the ZFT system we have used, the annealing model of *Galbraith and Laslett* [1997] with the annealing parameters proposed by *Rahn et al*. [2004]. We acknowledge that more elaborate models exist both for AFT and AHe age predictions [e.g., *Flowers et al*., 2009; *Gautheron et al*., 2009; *Ketcham et al*., 2007], which take into account compositional controls on annealing/diffusion rates. However, as *Fillon and van der Beek* [2012] pointed out previously, the characteristics of the observational data set justify the use of the simpler age-prediction models. In particular, for the AHe data *Gibson et al*. [2007] and *Metcalf et al*. [2009] reported effective uranium concentrations of a few tens of ppm, which is within the range where the kinetic parameters of *Farley* [2000] can be used [*Flowers et al*., 2009; *Gautheron et al*., 2009]. As concerns the AFT data, *Gibson et al*. [2007], *Metcalf et al*. [2009], and *Sinclair et al*. [2005] reported kinetic indicators close to that of Durango apatite, on which the kinetic parameters of *Stephenson et al*. [2006] have been calibrated. Moreover, the rapid cooling inferred from the age-elevation profiles (cf. section 2.3) will minimize any compositional effects on the AFT and AHe ages.

To evaluate the consistency of the restoration with the observed data, predicted thermochronological ages at the sampling location are extracted by interpolation and are compared to the observed ages. An objective function

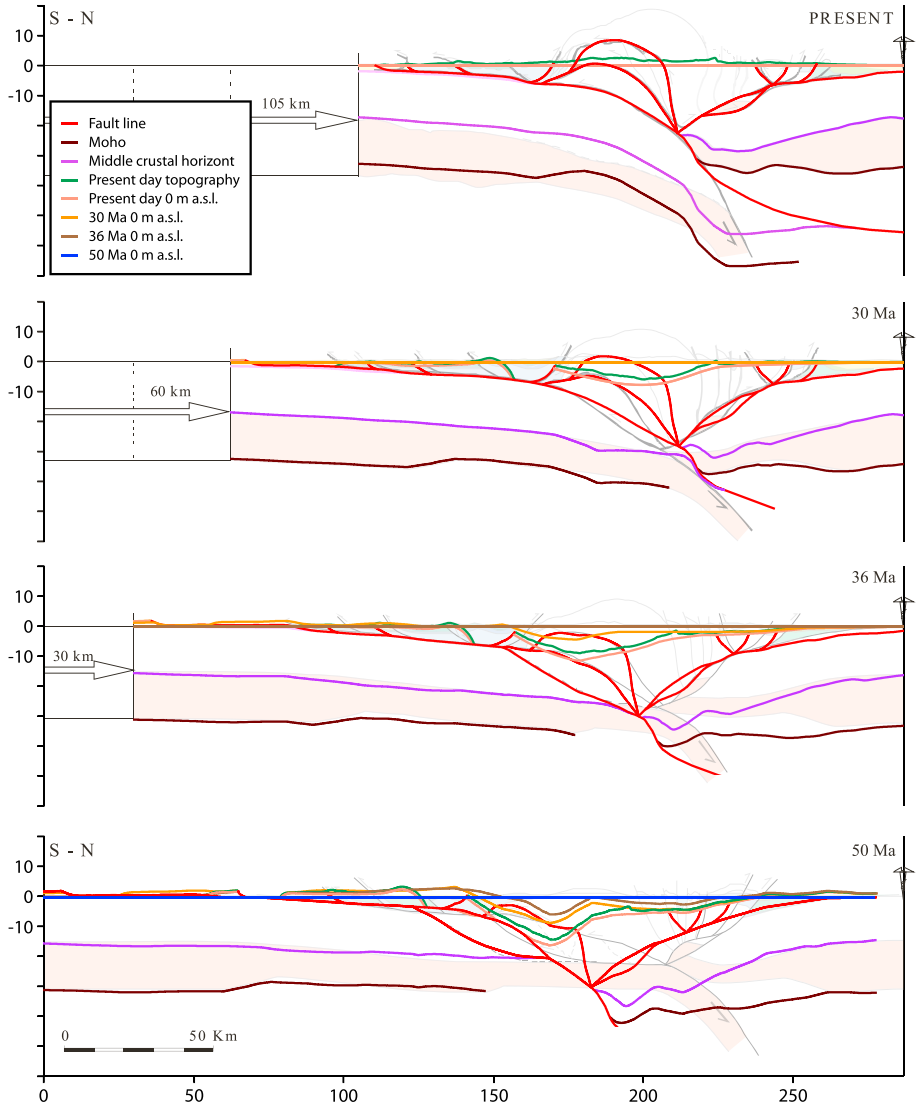

Figure 5. Result of the structural-kinematic modeling using 2D-Move™ for the same four time slices as shown in Figure 2. For comparison, the resulting crustal-scale geometry is plotted on top of the section restoration by *Muñoz* [1992] and *Beaumont et al.* [2000].

that takes into account the error on the observed ages allows quantifying the fit between the predicted and observed ages [*Glotzbach et al.*, 2011]. The resolution with which the input parameters of the forward models are constrained could, in principle, be assessed by inverse modeling [cf. *Braun et al.*, 2012; *Glotzbach et al.*, 2011; *Valla et al.*, 2010], but these require running large numbers of individual forward models with slightly varying parameters, which is not possible in this case due to the complexity of the structural-kinematic model.

For the available K-feldspar $^{40}Ar/^{39}Ar$ data, we have used the thermal histories predicted by multidiffusion domain modeling presented in *Metcalf et al.* [2009]. We compare these *t-T* paths qualitatively to the *t-T* paths extracted from our PECUBE models.

4. Results

4.1. Structural-Kinematic Modeling Results

The objective of the structural-kinematic modeling was to reproduce the section restoration presented by *Muñoz* [1992], in order to verify that it can be quantitatively balanced and to derive a set of velocity fields describing the movement of the crustal blocks through time.

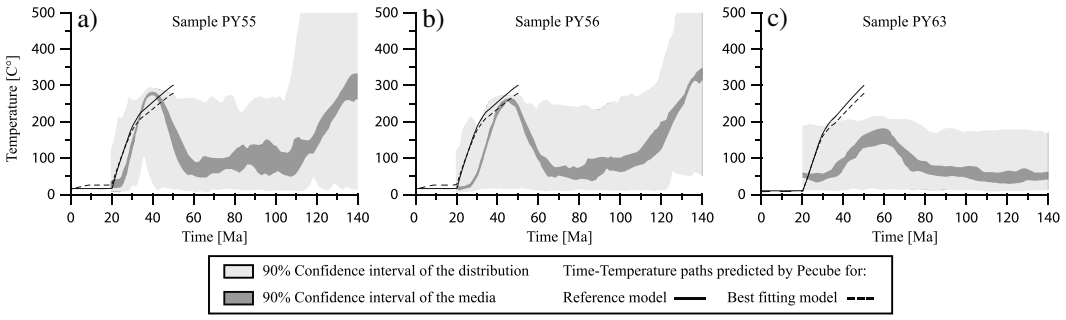

Figure 6. Predicted *t-T* paths plotted against the *t-T* paths inferred by *Metcalf et al.* [2009] from K-feldspar $^{40}Ar/^{39}Ar$ thermochronometry for three samples in the Maladeta unit [modified from *Metcalf et al.*, 2009].

The results of the modeling are compared with the original restoration in Figure 5. The model matches the restoration well for the 30 Ma and the 36 Ma time slices, except for the detailed geometry of the Axial Zone thrust sheets discussed below, but for the 50 Ma time slice, the mismatch becomes significant. The *Muñoz* [1992] restoration implies internal deformation of the Orri thrust sheet between 36 Ma and 50 Ma, thinning and elongating it significantly during retrodeformation. As a result, our model requires less convergence for the restoration of the Orri thrust sheet than the original reconstruction. Moreover, the *Muñoz* [1992] restoration implies 20% thickening of the Nogueres thrust sheet by internal deformation between 50 Ma and 60 Ma. Due to the accumulation of internal deformation and the uncertainties arising from the drawing method, such as the small changes in the area of crustal blocks, we could not restore the section beyond its 50 Ma state.

4.2. Thermokinematic Modeling Results

All the presented thermokinematic models utilize the same set of displacement fields derived from the structural-kinematic modeling. Material and thermal properties used in the thermokinematic modeling are given in Table 1. The *t-T* paths predicted for the locations of K-feldspar $^{40}Ar/^{39}Ar$ samples are plotted together with the *t-T* histories inferred by *Metcalf et al.* [2009] in Figure 6, while the predicted AFT and AHe ages are plotted together with the observed ages in age-elevation plots (Figures 7 and 9).

4.2.1. Reference Model

In the reference model, the present-day topography is kept constant through time, while adopted thermal parameters were the same as those used previously by *Fillon and van der Beek* [2012].

The reference model does not predict reset ZFT ages in the Nogueres and Marimaña massifs, but the two samples from the southern side of the Orri thrust sheet (from the Maladeta and Barruera units) have predicted ages of ~46 Ma, in contrast to observed ages of 49 and 104 Ma, respectively [*Sinclair et al.*, 2005]; the model therefore predicts these to have cooled from somewhat too high temperatures.

The *t-T* paths corresponding to the K-feldspar $^{40}Ar/^{39}Ar$ samples record rapid exhumation between 50 Ma and 20 Ma (Figure 6). The calculated *t-T* paths fit reasonably for the two lower elevation samples (PY55 and PY56) matching the peak burial temperature, while for the third sample (PY63), the predicted peak burial temperature is much higher than that extracted from the original data.

The AFT and AHe ages predicted by the reference model (Figure 7) for the profiles in the Axial Zone line up along subvertical trends and show ages between 33 and 27 Ma and between 26 and 22 Ma, respectively, caused by very rapid exhumation. This rapid exhumation results from underplating of the Nogueres and Orri thrust sheets by the Rialp thrust sheet between 36 and 20 Ma (Figure 5; cf. supporting information for details). For the Lacourt profile, the reference model predicts AFT ages around 50 Ma; the samples in this area have been exhumed from shallow depths and are only partially reset.

While predicted AFT ages from the Nogueres block (Figure 7a) are systematically older than the observed ages for the reference model, the predictions fit the Maladeta and Marimaña profile data reasonably well, especially for the samples taken from higher elevations (Figures 7b and 7c). For the Lacourt profile, the AFT-age predictions also fit the observed ages well (Figure 7c). Overall, 15 out of 40 AFT ages fit the observed

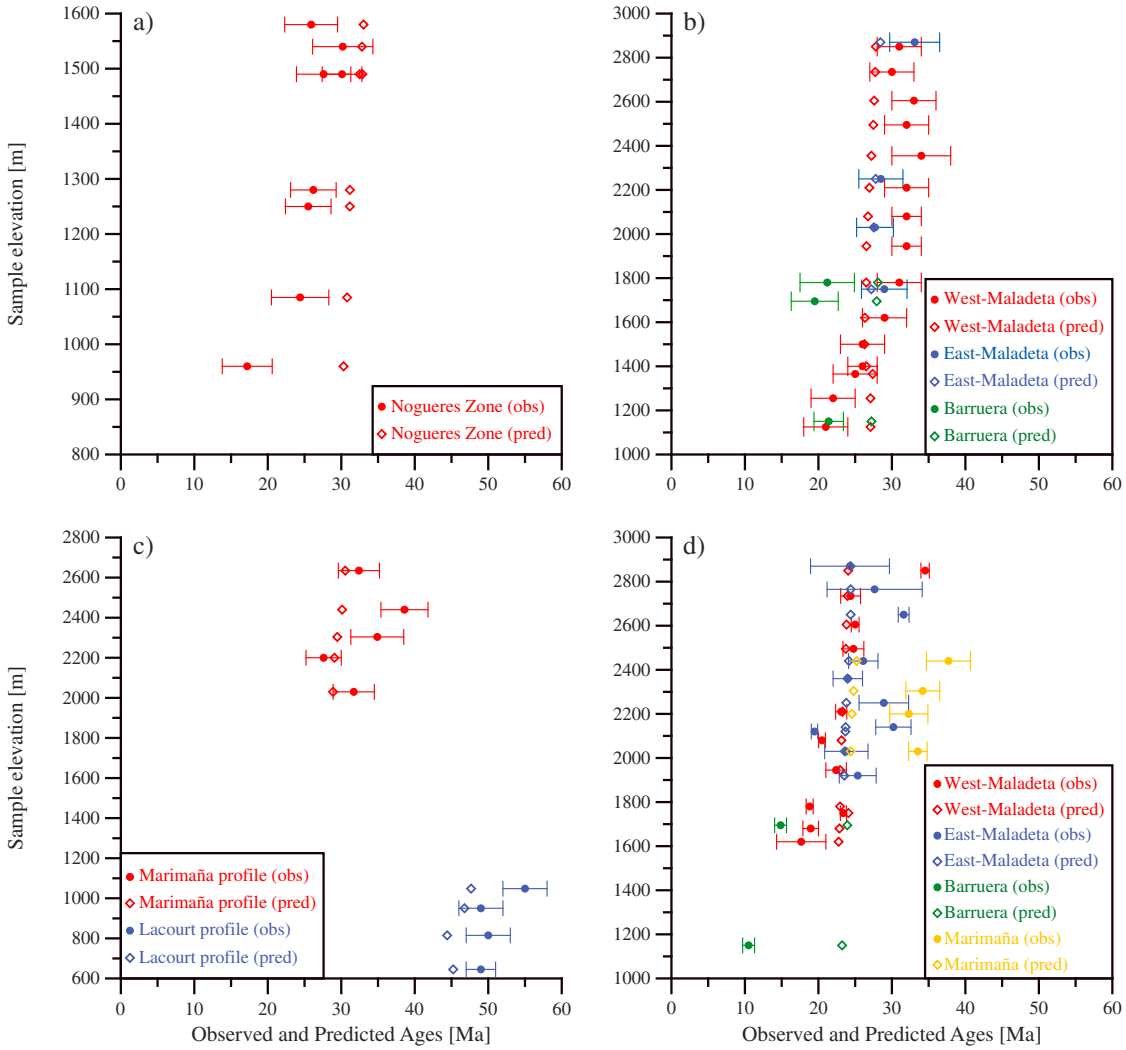

Figure 7. Comparison of predicted (solid symbols) and observed (open symbols with error bars) low-temperature thermochronologic ages for the reference model: (a) AFT data from the Nogueres Zone, (b) AFT data from Maladeta and Barruera, (c) AFT data from Marimaña and Lacourt, and (d) AHe data from Maladeta, Marimaña and Barruera. See Figures 1 and 3 for locations of sampling profiles.

ages to within 1σ error and 28 to within 2σ. The fit to the AHe data is less satisfactory, with only 8 out of 27 AHe ages fitted to within 1σ.The predictions of the reference model fit the higher-elevation AHe samples reasonably well, but they are systematically older than the observed ages for the lower elevation samples (Figure 7d). The predicted ages are significantly younger than the measured AHe ages from the Marimaña profile, as well as some from the East Maladeta profile reported in *Gibson et al.* [2007], suggesting that these data might be problematic (see also section 2.3).

In summary, the reference model predicts exhumation from somewhat too high temperatures for the ZFT data and one K-feldspar $^{40}Ar/^{39}Ar$ sample, suggesting that it either overpredicts the amount of exhumation or that the adopted thermal structure is not optimal. It also systematically overpredicts AFT and AHe ages for the lower elevation samples (with the exception of the Lacourt profile), while fitting the higher-elevation samples. This discrepancy may point to significant changes in topography between the active orogenic phase and the present day. We address both these issues in the following sections.

4.2.2. Parameter Sensitivity Analysis

We have carried out a simple sensitivity analysis to test whether we can improve the fit of the high-temperature (K-feldspar $^{40}Ar/^{39}Ar$ and ZFT) thermochronometers, while not deteriorating the fit of the low-temperature (AFT and AHe) thermochronometers. We have varied the crustal heat production and the basal

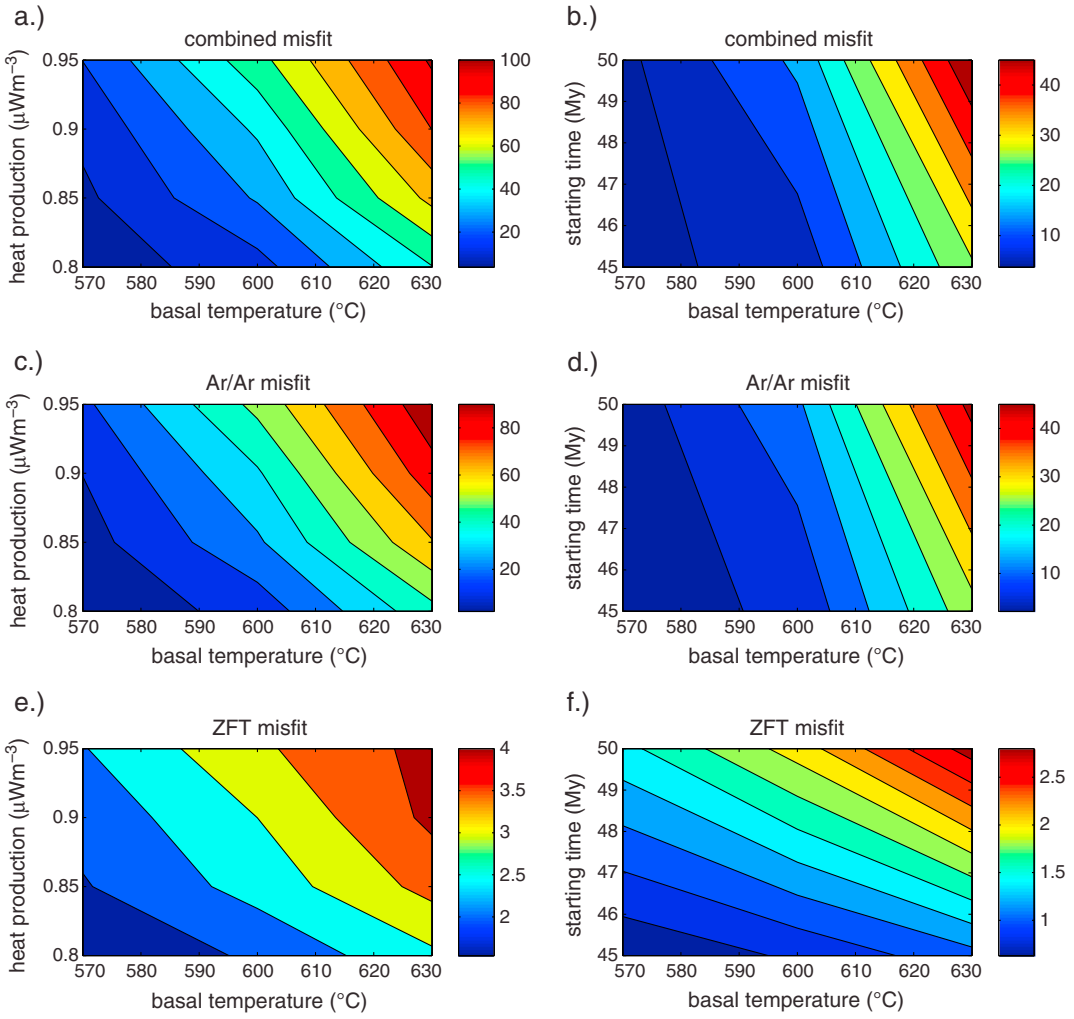

Figure 8. Contour plots showing the result of the sensitivity analysis as the misfit between observed and predicted thermochronologic ages according to equation (1). (a, b) Combined high-temperature data (K-feldspar $^{40}Ar/^{39}Ar$ and ZFT); (c, d) K-feldspar $^{40}Ar/^{39}Ar$ data only; (e, f) ZFT data only. Misfit is shown as function of basal temperature and heat production in Figures 8a, 8c, and 8e and as function of basal temperature and model starting time in Figures 8b, 8d, and 8f.

temperature while keeping the surface heat flow and the corresponding geothermal gradient close to the present-day values of 70 mW m^{-2} and 33°C km^{-1} measured in the foreland basins [e.g., *Fernandez and Banda*, 1989; *Fernandez et al.*, 1998].

The time-temperature models extracted from K-feldspar $^{40}Ar/^{39}Ar$ degassing experiments by *Metcalf et al.* [2009] show an onset of rapid cooling at around 45 Ma rather than 50 Ma (Figure 6). To test whether this apparent misfit between the observed and predicted onset of exhumation can be reduced, we have also run a set of models where we have modified the starting time to be 45 Ma, while adjusting the velocities for the first phase accordingly.

To evaluate the difference between the modeled and observed ages quantitatively and thus find the best fitting thermal parameters, we have used the objective function defined by *Glotzbach et al.* [2011]:

$$\mu = \sum_{i=1}^{n} \left(\frac{m_i - o_i}{\sigma_i} \right)^2 \quad (1)$$

where μ is the misfit value, n is the number of data points, and for each data point i, o_i is the observed value, m_i is the modeled value, and σ_i is the observed error. The results of the parameter test are presented for the high-temperature data in Figure 8; a full set of misfit values can be found in the supporting information (Table S2). Note, however, that the overall misfit is strongly controlled by the misfit to the AHe data.

The high-temperature data clearly suggest a cooler thermal structure than our initial guess: models with a basal temperature of 570°C and crustal heat production of 0.8 $\mu W\,m^{-3}$ provide the best fits to both the ZFT and the $^{40}Ar/^{39}Ar$ data; there is a strong positive correlation between misfit and both basal temperature and heat production. Interestingly, the ZFT data seem to prefer the later onset of exhumation (45 Ma) although this is not so clearly shown by the $^{40}Ar/^{39}Ar$ data. The low-temperature data show more complex trends, but their dependence on the thermal structure is less pronounced than that of the high-temperature data.

4.2.3. Topographic Evolution Scenario

In an attempt to improve our predictions for the lower elevation AFT and AHe samples, we have implemented the topographic evolution scenario suggested by *Coney et al*. [1996] and *Fitzgerald et al*. [1999]. In this scenario, the Ebro foreland basin and the South Pyrenean Unit were backfilled and buried by late-orogenic continental conglomerates in the late Eocene to Oligocene. *Coney et al*. [1996] suggested that, starting in the late Miocene, the Pyrenees were reexhumed by erosional excavation to the present relief. Recently, *Fillon and van der Beek* [2012] quantified the timing and amount of backfilling from thermokinematic modeling of the same AFT and AHe data set as that used here. They propose that the sediments gradually filled the valleys of the prowedge up to about 2.6 km elevation between 40 Ma and 29 Ma. This valley fill remained stable until about 9 Ma, when the valleys were gradually reexcavated in response to regressive erosion. We have used the values provided by *Fillon and van der Beek* [2012] to model the topographic evolution.

The imposed changes in topography have little effect on the predicted high-temperature thermochronometers; the ZFT samples show only partially reset ages, and the *t-T* paths corresponding to the K-feldspar $^{40}Ar/^{39}Ar$ samples show very similar characteristics to those predicted by the reference model, in terms of the peak temperature experienced during the model time (Figure 6). However, the imposed topographic scenario significantly improves the fit of the predicted AFT ages in the Nogueres Zone (Figure 9a and Table S2). The improvement is also evident for some of the lower elevation samples from the Maladeta and Barruera profiles, while the fit of higher-elevation samples from the Maladeta and Marimaña massifs does not change dramatically (Figures 9b and 9c). For the samples from the Lacourt profile, north of the drainage divide, keeping the present-day topography constant throughout the modeled time period provides the best fit to the data. This is an expected outcome, as there is no evidence for synorogenic or postorogenic burial of the northern flank of the orogen. Imposing an evolving postorogenic topography also improves the fit of the AHe age predictions for most of the lower elevation samples in the Maladeta and Barruera profiles, although it increased the misfit for some of the higher-elevation samples (Figure 9d).

5. Discussion

5.1. Limitations of the Approach

Before starting the interpretation of our results, it is essential to discuss the limitations of the proposed method and explore their possible effects on our findings.

Most balanced section restorations are drawn by hand and minor inaccuracies can lead to inconsistencies in the shapes of crustal blocks. The eclectic shifting of the North Pyrenean subvertical faults through time (Figure 2) provides an example of the possible inconsistencies arising from the hand-drawn nature of the restoration. While the structural-kinematic models are internally consistent, they also represent a simplification with respect to the original hand-restored cross-section. However, the generation of a set of consistent, quantitative velocity fields is required for using PECUBE and implies the use of a quantitative restoration tool such as 2D-Move.

Movements along faults with highly complex geometries are modeled with simple shear. This simple algorithm models deformation of the hanging wall by moving each point by the same horizontal distance following a path parallel to the fault [*Waltham*, 1989; *White et al*., 1986]. The algorithm is generally applicable for a wide range of fault kinematics. However, the method is incapable of handling internal (pure-shear) deformation of the blocks. Processes such as internal thickening and thinning cannot be reproduced with this model. The reconstruction presented by *Muñoz* [1992] displays significant internal thickening of the Nogueres thrust sheet (Figure 2), preventing the assessment of the pre-50 Ma reconstruction.

The use of the vectorial sum of the displacements to calculate the velocity field in each of the time intervals means that it is impossible to separate the effect of rapid, short-lived faulting events from the effect of those

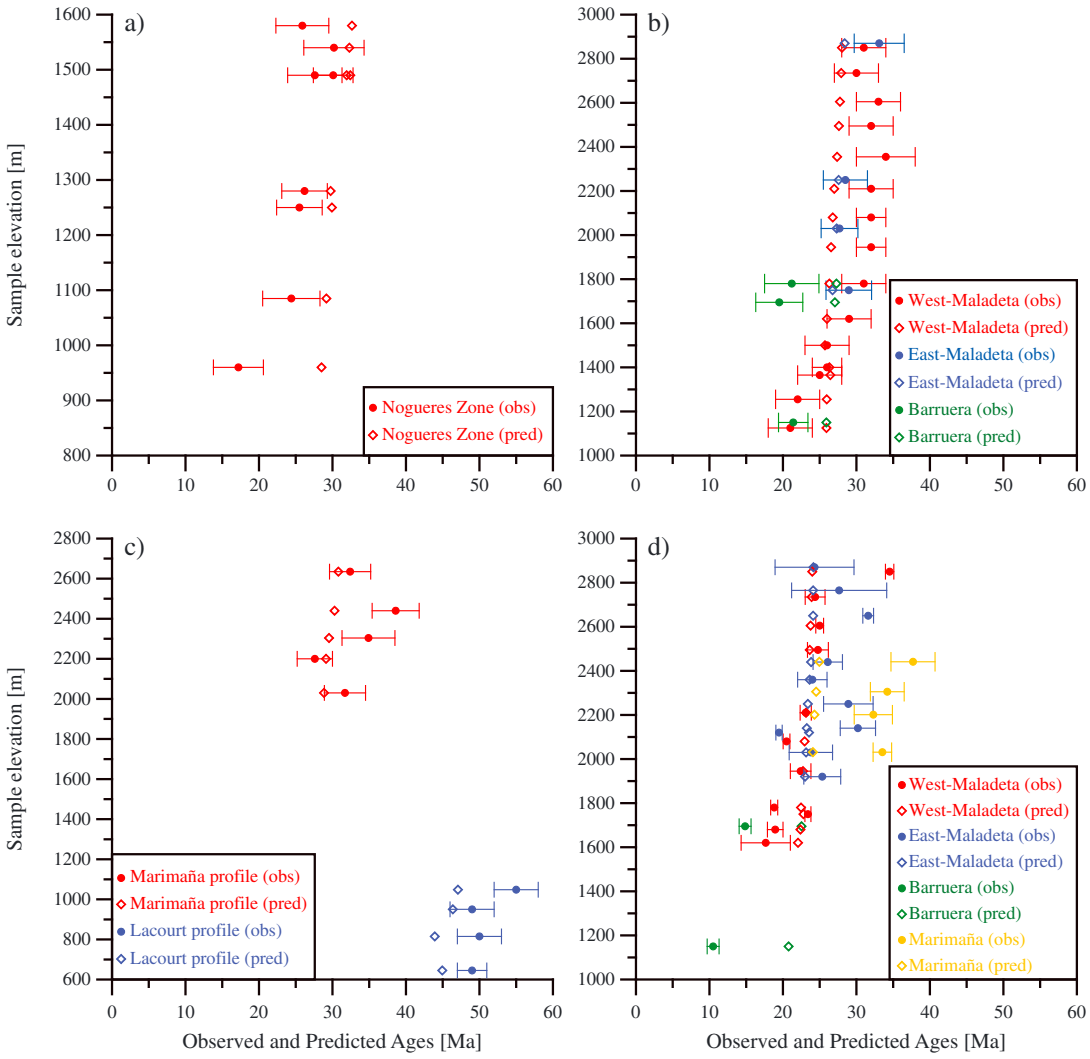

Figure 9. Comparison of predicted (solid symbols) and observed (open symbols with error bars) low-temperature thermochronologic ages for the best fitting model including postorogenic valley filling and reexcavation: (a) AFT data from the Nogueres Zone, (b) AFT data from Maladeta and Barruera, (c) AFT data from Marimaña and Lacourt, and (d) AHe data from Maladeta, Marimaña and Barruera. See Figures 1 and 3 for locations of sampling profiles.

that were active throughout the entire interval. This implies that if the time intervals of the restoration are long, a relatively short faulting event with high exhumation rates and a longer faulting event with lower exhumation rates will yield similar velocity fields. The length of the time intervals is limited by the temporal resolution of the modeled section restoration. In our case the temporal resolution of the section restoration is mainly dictated by the sedimentary record in the southern Pyrenean fold-and-thrust belt [*Muñoz*, 1992; *Beaumont et al.*, 2000].

While the age-prediction models—especially those for the low-temperature thermochronometers—are sensitive to the topographic changes, the paleotopography is hard to reconstruct with reasonable accuracy. In the presented case study, a very simple topographic evolution model has been implemented. The only currently available data that constrain the paleotopography of the Pyrenees suggest that they rose to their current elevation during the Eocene, between ~49 and ~41 Ma [*Huyghe et al.*, 2012]. We have therefore assumed the initial topography to be the same as the present-day topography. In addition, the evolution of morphology and relief is rather simple, as we only impose a changing minimum elevation of the topography. This means that the model linearly fills up or erodes the topography to the specified minimum elevation (see *Fillon and van der Beek* [2012] for a detailed discussion). Published provenance data for the preserved late-orogenic conglomerates suggest that planform drainage patterns have been relatively stable since the

Eocene on the southern flank of the Pyrenees [*Vincent*, 2001], and while there is no such evidence from the northern flank, the limited tectonic activity of the retrowedge also supports our simplified topographic evolution history.

Finally, it is necessary to point out that velocity fields derived with the same method from a different restoration could also provide predictions that would fit the observations. This nonuniqueness means that by using the method, it is possible to invalidate a restoration, but it is not possible to tell if a restoration that is consistent with the thermochronological data is absolutely correct. To use the words of *Oreskes et al*. [1994], "confirming observations do not demonstrate the veracity of a model hypothesis, they only support its probability."

5.2. Viability of the Section Reconstruction

It is essential to show that the section reconstruction is kinematically viable, before proceeding with the thermokinematic modeling and the evaluation of its consistency with the available thermochronological data.

In our case study, we had to make a number of minor modifications on the present-day time slice in order to be able to reproduce the general features of the 30 Ma and 36 Ma time slices of the section restoration (Figure 5). A detailed description of these modifications can be found in the supporting information. The internal deformation of the Orri thrust sheet implied by the section restoration between 36 Ma and 50 Ma made it difficult to reproduce the 50 Ma time slice with high accuracy. The elongation and thinning of the Orri thrust sheet on the original restoration resulted in more displacement along the basal decollement and significantly more contraction along the section than we infer from our section balancing (Figure 5). Despite the obvious discrepancies between the original restoration and our modeling, we have included the 50 Ma time slice in our thermokinematic modeling, as it captures the general features (e.g., the juxtaposition of the Orri and the Rialp blocks and the shallow position of the Orri thrust sheet) reasonably well. The inclusion of the 50 Ma time slice is important for the thermokinematic modeling, as it is required to predict the ages of the available high-temperature (ZFT and K-feldspar $^{40}Ar/^{39}Ar$) thermochronometers.

The 20% thickening of the Nogueres thrust sheet resulting from internal deformation between 50 Ma and 60 Ma (Figure 2) prevents the assessment of the section reconstruction beyond the 50 Ma time slice.

5.3. Implications of the Thermokinematic Modeling

Despite its limitations, the proposed method is capable of quantitatively evaluating a section restoration using both low- and high-temperature thermochronology data, providing an independent test on the consistency of both data sets. In case of the Pyrenees, the different deformation events are very well constrained owing to the large amount of geological and geophysical data and the unusually well-preserved thrust structures and related synorogenic sediments. In other geological settings, the method described here can help to test different hypotheses on the timing of deformation phases, or on structural interpretations, by quantitative comparison of different scenarios with available thermochronology data sets.

In our case study, the kinematic history inferred from the balanced section restoration is compatible with the available thermochronological data sets. The two predicted reset ZFT ages are not significantly younger than the model time suggesting that they might be only partially reset; a feature that is notoriously difficult to identify, as ZFT data usually do not include a kinetic parameter. Moreover, reset ZFT ages have been reported locally from Axial Zone massifs to the east and west of our study area (e.g., Canigou, Néouvieille) [cf. *Whitchurch et al*., 2011, and references therein]. Out of the three *t-T* paths inferred from K-feldspar $^{40}Ar/^{39}Ar$ thermochronometry by *Metcalf et al*. [2009], two (PY55 and PY56, from elevations of 1400 m and 1760 m, respectively; Figures 6a and 6b) are in good agreement with the model predictions. However, while our model predicts similar maximum reheating (~280°C) for all three samples, the results of *Metcalf et al*. [2009] imply significantly lower maximum reheating (~175°C) for the highest-elevation sample (PY63 from an elevation of 2850 m; Figure 6c). Such a large difference in the maximum temperature experienced during burial would imply an unrealistically high geothermal gradient of ~100°C/km, questioning the validity of the *t-T* path inferred from sample PY63. As *Metcalf et al*. [2009] noted, the Ar-release spectrum of this sample was not very well fit by the thermal model. Our models point to an onset of rapid exhumation at around 45 Ma rather than 50 Ma.

The predicted low-temperature thermochronometric ages generally show a reasonable fit with the observations, except for lower elevation samples from the Axial Zone (Figure 7). We have therefore included the postorogenic topographic evolution scenario initially proposed by *Coney et al*. [1996], using the timing and topographic constraints inferred by *Fillon and van der Beek* [2012]. According to this model, the southern flank of the Pyrenees was gradually buried in syntectonic sediments by 29 Ma up to an elevation of 2.6 km, before being reexcavated again after 9 Ma. Such burial affects the lower elevation samples significantly while having very little effect on samples from higher elevations. With this scenario, the thermokinematic modeling yielded AFT and AHe ages fitting both the higher- and the lower elevation samples of the Axial Zone reasonably well (Figure 9). It is also consistent with thermal-history models for low-elevation samples derived from track-length data [*Metcalf et al*., 2009].

6. Conclusions

We have presented a method that allows quantitative comparison of orogen kinematics inferred from balanced section restorations with independent thermochronological data sets. We have applied our method to the balanced section restoration presented by *Muñoz* [1992] and *Beaumont et al*. [2000] for the Central Pyrenees as a case study. Our structural-kinematic modeling could reproduce the section restoration with high accuracy up to the 36 Ma time slice and with limited accuracy up to the 50 Ma time slice. The thermochronometric ages predicted by the modeling are generally in reasonably good agreement with both the high- and low-temperature thermochronology data available in the Central Pyrenees; hence, we conclude that the restoration is to a first order consistent with these data sets. The high-temperature data suggest a somewhat later onset of underthrusting and rapid exhumation, as well as a somewhat cooler crustal thermal structure, than what we initially imposed. The fit of the low-temperature data improved by taking into account late-stage burial and reexcavation of the southern flank of the Pyrenean wedge using the topographic evolution scenario presented by *Fillon and van der Beek* [2012]. The method can be applied on section restorations from other orogens as well, with the aim of evaluating the consistency of the restoration with an independent data set. We propose that the method can also be used to improve constraints on the timing of deformation phases along a restored balanced cross section.

Acknowledgments
This study is supported by the Norwegian Research Council that funded the Norwegian component of the European Science Foundation Eurocores TOPO-Europe project PyrTec. We thank Jean Braun, Charlotte Fillon, and Josep Anton Muñoz for helpful discussions and comments on various stages of the work, and Paul Fitzgerald and Hugh Sinclair for providing details on sample locations. The Bergen Center of Computational Science is acknowledged for access to computational infrastructure. Detailed and insightful comments by James Metcalf and Peter DeCelles on the manuscript, as well as by an anonymous reviewer on an earlier version, helped to improve it significantly.

References

Beaumont, C., J. A. Muñoz, J. Hamilton, and P. Fullsack (2000), Factors controlling the Alpine evolution of the Central Pyrenees inferred from a comparison of observations and geodynamical models, *J. Geophys. Res.*, *105*, 8121–8145.
Braun, J. (2002), Quantifying the effect of recent relief changes on age-elevation relationships, *Earth Planet. Sci. Lett.*, *200*, 331–343.
Braun, J. (2003), Pecube: A new finite-element code to solve the 3D heat transport equation including the effects of a time-varying finite amplitude surface topography, *Comput. Geosci.*, *29*, 787–794.
Braun, J., P. van der Beek, and G. E. Batt (2006), *Quantitative Thermochronology. Numerical Methods for the Interpretation of Thermochronological Data*, 258 pp, Cambridge Univ. Press, Cambridge, U. K.
Braun, J., P. van der Beek, P. Valla, X. Robert, F. Herman, C. Glotzbach, V. Pedersen, C. Perry, T. Simon-Labric, and C. Prigent (2012), Quantifying rates of landscape evolution and tectonic processes by thermochronology and numerical modeling of crustal heat transport using PECUBE, *Tectonophysics*, *524-525*, 1–28.
Capote, R., J. A. Muñoz, J. L. Simon, C. L. Liesa, and L. E. Arlegui (2002), Alpine tectonics I: The alpine system north of the Betic Cordillera, in *The Geology of Spain*, edited by W. Gibbon and T. Moreno, pp. 367–400, The Geological Society, London, U. K.
Coney, P. J., J. A. Muñoz, K. R. McClay, and C. A. Evenchick (1996), Syntectonic burial and post-tectonic exhumation of the southern Pyrenees foreland fold-thrust belt, *J. Geol. Soc. London*, *153*, 9–16.
Cook, F. A., J. L. Varsek, R. M. Clowes, E. R. Kanasewich, C. S. Spencer, R. R. Parrish, R. L. Brown, S. D. Carr, B. J. Johnson, and R. A. Price (1992), Lithoprobe crustal reflection cross section of the southern Canadian Cordillera, 1, Foreland thrust and fold belt to Fraser River Fault, *Tectonics*, *11*, 12–35.
Dahlstrom, C. D. A. (1969), Balanced cross sections, *Can. J. Earth Sci.*, *6*, 743–757.
DeCelles, P. G., D. M. Robinson, J. Quade, T. P. Ojha, C. N. Garzione, P. Copeland, and B. N. Upreti (2001), Stratigraphy, structure, and tectonic evolution of the Himalayan fold-thrust belt in western Nepal, *Tectonics*, *20*, 487–509.
Egan, S. S., S. Kane, T. S. Buddin, G. D. Williams, and D. Hodgetts (1999), Computer modelling and visualisation of the structural deformation caused by movement along geological faults, *Comput. Geosci.*, *25*, 283–297.
Farley, K. A. (2000), Helium diffusion from apatite: General behavior as illustrated by Durango fluorapatite, *J. Geophys. Res.*, *105*, 2903–2914.
Fernandez, M., and E. Banda (1989), An approach to the thermal field in northeastern Spain, *Tectonophysics*, *164*, 259–266.
Fernandez, M., I. Marzan, A. Correia, and E. Ramalho (1998), Heat flow, heat production, and lithospheric thermal regime in the Iberian Peninsula, *Tectonophysics*, *291*, 29–53.
Fillon, C., and P. van der Beek (2012), Post-orogenic evolution of the southern Pyrenees: Constraints from inverse thermo-kinematic modelling of low-temperature thermochronology data, *Basin Res.*, *24*, 418–436.
Fillon, C., R. S. Huismans, P. van der Beek, and J. A. Muñoz (2013), Syntectonic sedimentation controls on the evolution of the southern Pyrenean fold-and-thrust belt: Inferences from coupled tectonic-surface processes models, *J. Geophys. Res. Solid Earth*, *118*, 5665–5680, doi:10.1002/jgrb.50368.

Fitzgerald, P. G., J. A. Muñoz, P. J. Coney, and S. L. Baldwin (1999), Asymmetric exhumation across the Pyrenean orogen: Implications for the tectonic evolution of a collisional orogen, *Earth Planet. Sci. Lett.*, *173*, 157–170.
Flowers, R. M., R. A. Ketcham, D. L. Shuster, and K. A. Farley (2009), Apatite (U-Th)/He thermochronometry using a radiation damage accumulation and annealing model, *Geochim. Cosmochim. Acta*, *73*, 2347–2365.
Galbraith, R., and G. Laslett (1997), Statistical modeling of thermal annealing of fission tracks in zircon, *Chem. Geol.*, *140*, 123–135.
Gautheron, C., L. Tasson-Got, J. Barbarand, and M. Pagel (2009), Effect of alpha-damage annealing on apatite (U-Th)/He thermochronology, *Chem. Geol.*, *266*, 157–170.
Gibson, M., H. D. Sinclair, G. J. Lynn, and F. M. Stuart (2007), Late- to post-orogenic exhumation of the Central Pyrenees revealed through combined thermochronological data and modelling, *Basin Res.*, *19*, 323–334.
Glotzbach, C., P. van der Beek, and C. Spiegel (2011), Episodic exhumation of the Mont Blanc massif, Western Alps: Constraints from numerical modelling of thermochronology data, *Earth Planet. Sci. Lett.*, *304*, 417–430.
Green, P., I. Duddy, G. Laslett, K. Hegarty, A. Gleadow, and J. F. Lovering (1989), Thermal annealing of fission tracks in apatite 4. Quantitative modelling techniques and extension to geological timescales, *Chem. Geol.*, *79*, 155–182.
Herman, F., et al. (2010), Exhumation, crustal deformation, and thermal structure of the Nepal Himalaya derived from the inversion of thermochronological and thermobarometric data and modeling of the topography, *J. Geophys. Res.*, *115*, B06407, doi:10.1029/2008JB006126.
Huyghe, D., F. Mouthereau, and L. Emmanuel (2012), Oxygen isotopes of marine mollusc shells record Eocene elevation change in the Pyrenees, *Earth Planet. Sci. Lett.*, *345-348*, 131–141.
Ketcham, R. A., A. Carter, R. A. Donelick, J. Barbarand, and A. J. Hurford (2007), Improved modeling of fission-track annealing in apatite, *Am. Mineral.*, *92*, 789–798.
Lock, J., and S. Willett (2008), Low-temperature thermochronometric ages in fold-and-thrust belts, *Tectonophysics*, *456*, 147–162.
Long, S., N. McQuarrie, T. Tobgay, and D. Grujic (2011), Geometry and crustal shortening of the Himalayan fold-thrust belt, eastern and central Bhutan, *Geol. Soc. Am. Bull.*, *123*, 1427–1447.
Long, S. P., N. McQuarrie, T. Tobgay, I. Coutand, F. J. Cooper, P. W. Reiners, J.-A. Wartho, and K. V. Hodges (2012), Variable shortening rates in the eastern Himalayan thrust belt, Bhutan: Insights from multiple thermochronologic and geochronologic data sets tied to kinematic reconstructions, *Tectonics*, *31*, TC5004, doi:10.1029/2012tc003155.
McQuarrie, N. (2002), The kinematic history of the central Andean fold-thrust belt, Bolivia: Implications for building a high plateau, *Geol. Soc. Am. Bull.*, *14*, 950–963.
McQuarrie, N., J. B. Barnes, and T. A. Ehlers (2008), Geometric, kinematic, and erosional history of the central Andean Plateau, Bolivia (15–17°S), *Tectonics*, *27*, TC3007, doi:10.1029/2006TC002054.
Metcalf, J. R., P. G. Fitzgerald, S. L. Baldwin, and J. A. Muñoz (2009), Thermochronology of a convergent orogen: Constraints on the timing of thrust faulting and subsequent exhumation of the Maladeta Pluton in the Central Pyrenean Axial Zone, *Earth Planet. Sci. Lett.*, *287*, 488–503.
Muñoz, J. A. (1992), Evolution of a continental collision belt: ECORS Pyrenees crustal balanced cross section, in *Thrust Tectonics*, edited by K. R. McClay, pp. 235–246, Chapman & Hall, London, U. K.
Muñoz, J. A., A. Martínez, and J. Vergés (1986), Thrust sequences in the Spanish Pyrenees, *J. Struct. Geol.*, *8*, 399–405.
Oreskes, N., K. Shrader-Frechette, and K. Belitz (1994), Verification, validation, and confirmation of numerical models in the earth sciences, *Science*, *263*, 641–646.
Puigdefabregas, C., J. A. Muñoz, and M. Marzo (1986), Thrust belt development in the eastern Pyrenees and related depositional sequences in the southern foreland basin, in *Foreland Basins*, vol. 8, edited by P. A. Allen and P. Homewood, pp. 229–246, Int. Assoc. Sedimentol. Spec., Blackwell Publishing Ltd., Oxford, U. K., doi:10.1002/9781444303810.ch12.
Puigdefabregas, C., J. A. Muñoz, and J. Vergés (1992), Thrusting and foreland basin evolution in the southern Pyrenees, in *Thrust Tectonics*, edited by K. R. McClay, pp. 247–254, Chapman & Hall, London, U. K.
ECORS Pyrenees Team (1988), The ECORS deep reflection seismic survey across the Pyrenees, *Nature*, *331*, 508–511.
Rahn, M. K., M. T. Brandon, G. E. Batt, and J. I. Garver (2004), A zero-damage model for fission track annealing in zircon, *Am. Mineral.*, *89*, 473–484.
Reiners, P. W., and M. T. Brandon (2006), Using thermochronology to understand orogenic erosion, *Ann. Rev. Earth Planet. Sci.*, *34*, 419–466.
Robert, X., P. van der Beek, J. Braun, C. Perry, and J. L. Mugnier (2011), Control of detachment geometry on lateral variations in exhumation rate in the Himalaya: Insights from low-temperature thermochronology and numerical modeling, *J. Geophys. Res.*, *116*, B05202, doi:10.1029/2010JB007893.
Robinson, D. M., P. G. DeCelles, and P. Copeland (2006), Tectonic evolution of the Himalayan thrust belt in western Nepal: Implications for channel flow models, *Geol. Soc. Am. Bull.*, *118*, 865–885.
Roest, W. R., and S. P. Srivastava (1991), Kinematics of the plate boundaries between Eurasia, Iberia and Africa in the North Atlantic from the late Cretaceous to the present, *Geology*, *19*, 613–616.
Rosenbaum, G., G. S. Lister, and C. Duboz (2002), Relative motions of Africa, Iberia and Europe during Alpine orogeny, *Tectonophysics*, *359*, 117–129.
Roure, F., F. Bergerat, B. Damotte, J.-L. Mugnier, and R. Polino (1996), The ECORS-CROP alpine seismic traverse, Mémoire de la Société Géologique de France, 170, 113 pp., Société géologique de France, Paris, France.
Rushlow, C. R., J. B. Barnes, T. A. Ehlers, and J. Vergés (2013), Exhumation of the southern Pyrenean fold-thrust belt (Spain) from orogenic growth to decay, *Tectonics*, *32*, 843–860, doi:10.1002/tect.20030.
Schmid, S. M., O. A. Pfiffner, N. Froitzheim, G. Schönborn, and E. Kissling (1996), Geophysical-geological transect and tectonic evolution of the Swiss-Italian Alps, *Tectonics*, *15*, 1063–1064.
Séguret, M., and M. Daignières (1986), Crustal scale balanced cross sections from the Pyrenees: Discussion, *Tectonophysics*, *129*, 303–318.
Sinclair, H. D., M. Gibson, M. Naylor, and R. G. Morris (2005), Asymmetric growth of the Pyrenees revealed through measurement and modeling of orogenic fluxes, *Am. J. Sci.*, *305*, 369–406.
Stephenson, J., K. Gallagher, and C. C. Holmes (2006), A Bayesian approach to calibrating apatite fission track annealing models for laboratory and geological timescales, *Geochim. Cosmochim. Acta*, *70*, 5183–5200.
ter Voorde, M., C. H. de Bruijne, S. A. P. L. Cloetingh, and P. A. M. Andriessen (2004), Thermal consequences of thrust faulting: Simultaneous versus successive fault activation and exhumation, *Earth Planet. Sci. Lett.*, *223*, 395–413.
Valla, P. G., F. Herman, P. van der Beek, and J. Braun (2010), Inversion of thermochronological age-elevation profiles to extract independent estimates of denudation and relief history—I: Theory and conceptual model, *Earth Planet. Sci. Lett.*, *295*, 511–522.
Vergés, J., and J. A. Muñoz (1990), Thrust sequences in the southern Central Pyrenees, *Bull. Soc. Geol. Fr.*, *8*, 265–271.

Vincent, S. J. (2001), The Sis palaeovalley: A record of proximal fluvial sedimentation and drainage basin development in response to Pyrenean mountain building, *Sedimentology*, *48*, 1235–1276.
Vissers, R. L. M., and P. T. Meijer (2012), Iberian plate kinematics and Alpine collision in the Pyrenees, *Earth Sci. Rev.*, *114*, 61–83.
Waltham, D. (1989), Finite difference modelling of hangingwall deformation, *J. Struct. Geol.*, *11*, 433–437.
Waltham, D., and S. Hardy (1995), The velocity description of deformation. Paper 1: Theory, *Mar. Petrol. Geol.*, *12*, 153–163.
Whipp, D. M., T. A. Ehlers, A. Blythe, K. W. Huntington, K. Hodges, and D. W. Burbank (2007), Plio-Quaternary exhumation history of the central Nepalese Himalaya: 2. Thermokinematic and thermochronometer age prediction model, *Tectonics*, *26*, TC3003, doi:10.1029/2006TC001991.
Whitchurch, A. L., A. Carter, H. D. Sinclair, R. A. Duller, A. C. Whittaker, and P. A. Allen (2011), Sediment routing system evolution within a diachronously uplifting orogen: Insights from detrital zircon thermochronological analyses from the South-Central Pyrenees, *Am. J. Sci.*, *311*, 442–482, doi:10.2475/05.2011.03.
White, N. J., J. A. Jackson, and D. P. McKenzie (1986), The relationship between the geometry of normal faults and that of sedimentary layers in their hanging-walls, *J. Struct. Geol.*, *8*, 897–910.
Withjack, M. O., and E. T. Peterson (1993), Prediction of normal-fault geometries—A sensitivity analysis, *Am. Assoc. Petrol. Geol. Bull.*, *77*, 1860–1873.
Wolf, R. A., K. A. Farley, and D. M. Kass (1998), Modeling of the temperature sensitivity of the apatite (U-Th)/He thermochronometer, *Chem. Geol.*, *148*, 105–114.